Optimization of the perovskite cell in a bifacial two-terminal perovskite/silicon tandem module

Blom, Youri; Vogt, Malte Ruben; Isabella, Olindo; Santbergen, Rudi

DOI
10.1016/j.solmat.2025.113431

Publication date
2025

Document Version
Final published version

Published in
Solar Energy Materials and Solar Cells

Solar Energy Materials & Solar Cells 282 (2025) 113431

Contents lists available at ScienceDirect

Solar Energy Materials and Solar Cells

journal homepage: www.elsevier.com/locate/solmat

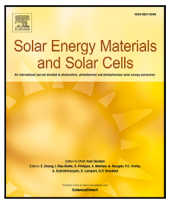

Optimization of the perovskite cell in a bifacial two-terminal perovskite/silicon tandem module

Youri Blom *, Malte Ruben Vogt, Olindo Isabella, Rudi Santbergen *

Delft University of Technology, Mekelweg 4, Delft, 2628CD, The Netherlands

ARTICLE INFO

Keywords:
Perovskite/silicon cells
Bifacial modules
Energy yield modeling
Energy losses

ABSTRACT

Bifacial perovskite/silicon solar cells can combine the advantages of tandem technology (high efficiencies) and bifacial modules (additional received irradiance from the rear) to increase the energy yield of photovoltaic (PV) systems further. In literature, it has already been shown that for two-terminal tandems this would require a lower bandgap energy (E_g) for the perovskite cell, as the rear irradiance increases the current in the bottom cell creating a current mismatch, if this is not considered during optimization. This work expands on bifacial two-terminal tandem optimization by considering aspects not included before. Besides the E_g, the thickness (d) of the perovskite is also optimized, as this also affects the current matching. Additionally, this work studies the trends in different energy losses of the PV module to better understand what affects the optimal perovskite cell. Our simulations show that the optimal E_g is 1.61–1.65 eV and the optimal d is 650–750 nm, which agrees with the observations in literature. The optimal E_g and d are mostly a trade-off between mismatch and thermalization losses, meaning that the mismatch losses should not be fully minimized. Additionally, the irradiance from the rear side is converted less efficiently than the front side irradiance due to larger thermalization and reflection losses. Therefore, the energy yield of bifacial tandem modules, compared to monofacial tandem ones, only increases for large ground albedo. Finally, our results show that the bifacial tandems have over a 25% gain in energy yield compared to bifacial single junction modules and up to 5% gain compared to monofacial tandem modules.

1. Introduction

The photovoltaic (PV) market is currently dominated by crystalline silicon (c-Si) solar cells [1], which have achieved a power conversion efficiency (PCE) of 27.3% [2], approaching their theoretical limit of 29.5% [3,4]. To further increase the energy yield (EY) per unit area, innovative technologies are required. One such approach is the use of double-junction solar cells, which have a theoretical PCE of over 40% [5]. Perovskite, with its excellent optical and electrical properties [6,7] and tunable bandgap energy [8], is a promising material for the top cell in these so-called *tandem* configurations. Combining perovskite with silicon in a tandem solar cell has already resulted in efficiencies well exceeding 30% [9–11], surpassing the theoretical limit of c-Si cells.

Another method to enhance the EY of PV systems is the use of bifacial modules, which can absorb additional light from the rear side, potentially increasing the energy yield of c-Si modules by up to 40% [12,13]. In 2023 bifacial modules had a market share of 50% and are projected to increase to 70% in 2028 [1].

Combining these approaches can lead to high-performance bifacial perovskite/silicon modules. This concept has been widely studied in literature [14–22], where it is shown that energy yield can be improved by relatively 20% compared to the monofacial tandem modules [14,18]. Similar studies have been done for bifacial all-perovskite tandem cells [23]. For monolithic two-terminal (2T) devices, it was found that the additional rear side irradiance can create a mismatch in current, as it is only absorbed in the silicon bottom cell. A common solution for this, is to lower the bandgap energy of the perovskite cell [14–20] or change the perovskite thickness [14,20,21] to enhance the absorption of the front-side irradiance in the perovskite layer.

Although existing studies are detailed and comprehensive, some aspects of bifacial tandem modules remain underexplored. Firstly, these studies often focus on energy yield or efficiency without discussing received irradiance or energy losses in the PV module. Our previous work [24] has introduced a method for quantifying different losses in a PV system. The observed trends can be better understood by analyzing the difference in losses between monofacial and bifacial modules. Secondly, the impact of perovskite thickness on its electrical

* Corresponding authors.
E-mail addresses: Y.Blom@tudelft.nl (Y. Blom), R.Santbergen@tudelft.nl (R. Santbergen).

https://doi.org/10.1016/j.solmat.2025.113431
Received 6 November 2024; Received in revised form 19 December 2024; Accepted 12 January 2025
Available online 22 January 2025

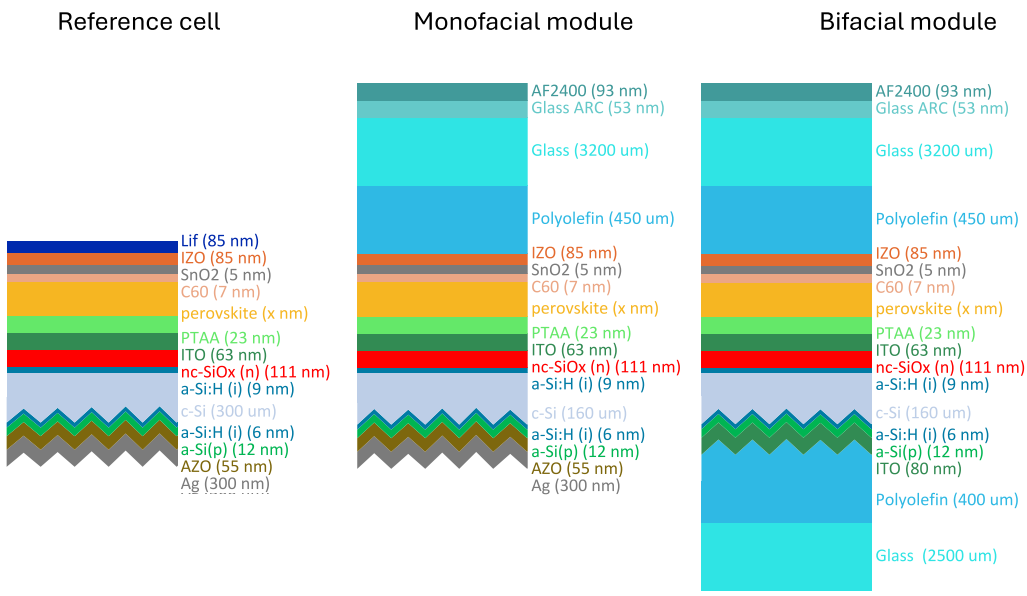

Fig. 1. The bifacial perovskite/silicon cell structure used in the simulations. The reference cell is adjusted by reducing the wafer thickness and adding glass and encapsulation. The bifacial modules are created by removing the silver layer and adding a second encapsulant layer. These structures are given as input to the optical model.

properties [25,26], in addition to its optical performance, should be considered when calculating energy yield. Finally, the wavelength-dependence of albedo reflection [27], which is often assumed to be wavelength-independent, is a crucial factor in energy yield simulations [28].

In this work, we optimize the design of the perovskite cell in a bifacial monolithic 2T tandem module under various conditions, addressing the aforementioned aspects. Using the 32.5% efficient perovskite silicon tandem cell from HZB [10] as a reference, we adjust the bandgap energy and thickness of the perovskite layer to maximize the energy yield of bifacial modules. Section 2 explains the methodology, Section 3 discusses the optimization for different scenarios, Section 4 presents the results, and Section 5 provides the conclusion.

2. Methodology

The simulations in this work are performed with the PVMD Toolbox [29], which is a modeling framework for PV systems based on the fundamental material properties and first principle physics. The energy yield is calculated by simulating the electricity production for each hour in the year. The calculation is divided into multiple steps that each simulate a different aspect of the PV system. These steps are carried out sequentially, where each step uses the results of the previous one. For this work, the optical and electrical simulations are the most relevant. The optical simulations are performed with GenPro [30], which employs the net radiation method [31]. The electrical properties of the cell are calculated by the Advanced Semiconductor Analysis (ASA) [32–34]. ASA simulates the current density–voltage (JV) curve of the solar cell for different temperatures and irradiance levels by solving the Poisson equation and continuity equations for electrons and holes. Then, we fit all JV curves with a one-diode equivalent circuit, consisting of five parameters, which are the photogenerated current (I_{ph}), the diode saturation current (I_0), the diode ideality factor (n), the shunt resistance (R_{sh}), and the series resistance (R_s). With all the fits, we make a calibrated lumped element method (CLEM) model, which outputs the value of each parameter for each temperature and irradiance level. The CLEM model is used in the energy yield simulation to reconstruct the IV curve for every hour in the year. A detailed description of all steps is presented in [29].

Since the work of Vogt et al. [29], the PVMD Toolbox has undergone several extensions and improvements. This section discusses the expansions that are relevant to this work.

2.1. Mounting condition model

The forward ray-tracing model LUX [35] is replaced by a backward ray-tracing model [36], which is computationally less expensive. This allows for faster calculation, making it more beneficial for an optimization study. The ray-tracing model calculates a so-called sensitivity map [35] that is required to calculate the absorbed irradiance. It includes the shading effects of modules on neighboring modules, as well as the effect of ground shading on albedo and rear-side irradiance. The ground reflectance is simulated by assuming a Lambertian scattering combined with the spectral reflectance of the ground material.

2.2. Spectral irradiance model

The absorbed irradiance in each solar cell of the PV module is calculated by combining the sensitivity map with a spectral irradiance map [35]. The irradiance distribution across the sky is calculated with the Perez model [37]. Originally, the Toolbox used SMARTS [38] to obtain the spectral irradiance. As SMARTS only calculates the direct beam irradiance, it has been replaced with the SBDART model [39], which provides the spectral distribution for both the direct and diffuse irradiance. This allows us to use a different spectrum for the different types of irradiances. The SBDART model also accounts for different air masses and cloud coverage.

3. Case study

As mentioned before, this work will show how to optimize the bandgap energy and thickness of the perovskite cell in a bifacial module. This section discusses the input conditions used and the method for varying the bandgap energy and thickness of the perovskite layer. Also, the different operating conditions under which the optimization is performed are discussed.

3.1. The design of the PV module

The module used for this work is based on the perovskite/silicon tandem cell from HZB [10] with a cell efficiency of 32.5%. The simulation of this cell in the Toolbox has been demonstrated in earlier work [40], where we showed that both the optical and electrical behavior of the cell can be accurately modeled. To perform energy yield

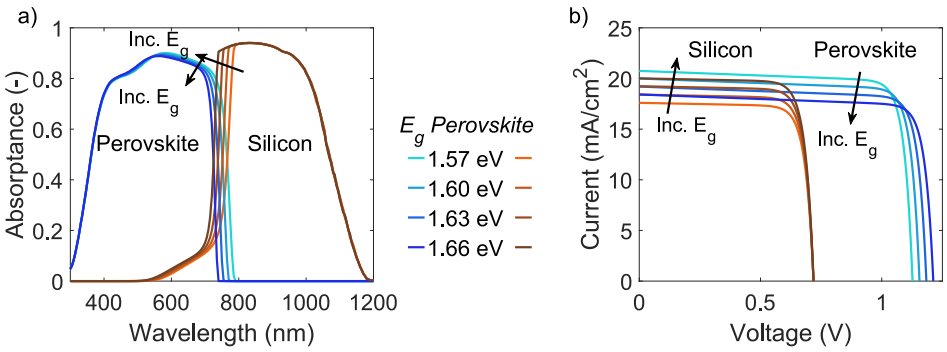

Fig. 2. The effect of changing the bandgap energy of perovskite on the absorptance in perovskite and silicon (a) and the JV curves of the subcells (b). For both figures, a perovskite thickness of 550 nm is used.

calculations at the module level, we added encapsulation and reduced the silicon thickness from 300 μm to 160 μm. Additionally, to convert the cell to a bifacial design, we replaced the silver layer at the back with another encapsulation layer. Fig. 1 provides an overview of the changes in the optical structure.

For the module simulation, 72 perovskite/silicon tandem cells (15.7 cm by 15.7 cm) are connected in series. Since a metal grid is necessary for current collection, a resistor is added to each cell to account for the ohmic interconnection. The resistor values are 1.3 mΩ for monofacial modules and 2.6 mΩ for bifacial modules, similar to the values reported by Jung et al. [41]. The higher resistance in bifacial cells is due to the metal grid being on both front and rear sides. Additionally, three bypass diodes are included in the module.

3.1.1. Adjusting the bandgap energy of perovskite

As previously discussed, bandgap engineering is the most common approach for achieving current matching in bifacial tandem devices. The bandgap energy (E_g) of the perovskite layer affects its complex refractive index ($N(\lambda)$), which in turn affects both the optical response, and the electrical performance of the perovskite subcell. Using measured data from Manzoor [8], we predict $N(\lambda)$ of perovskite absorber for arbitrary bandgap energies, utilizing the approach outlined in our prior work [42,43]. Fig. 2a shows the effect of varying E_g of the perovskite on the absorption profile of both absorber layers.

A larger E_g shifts the cut-off wavelength to shorter wavelengths, reducing the number of photons that can be absorbed. Consequently, the silicon cell's absorption increases as more photons pass through the perovskite and are absorbed by the silicon, resulting in lower short-circuit current density (J_{sc}) for the perovskite cell and higher J_{sc} for the silicon cell. In our electrical simulations, we also increase the E_g of the perovskite layer. This increases the open circuit voltage (V_{oc}) of the perovskite subcell accordingly. Fig. 2b presents the trends in both J_{sc} and V_{oc} as E_g varies.

3.1.2. Adjusting the perovskite's thickness

Another parameter that can be varied for achieving current matching, is the thickness of the perovskite layer. This parameter impacts both the optical and electrical performance of the solar cell [44]. Fig. 3 illustrates the different absorption profiles and JV curves for varying thicknesses. As the perovskite thickness increases, its absorption also increases as photons travel a longer distance. This effect is most noticeable in the wavelength range of 550–750 nm, as shown in Fig. 3a. Conversely, the absorptance in the silicon decreases in this wavelength range as thicker perovskite layers become less transparent.

Changes in perovskite thickness and absorption profiles also affect electrical performance, as shown in Fig. 3b. The most significant changes are in the J_{sc}, which increases for the perovskite cell and decreases for the silicon cell. However, the increase in J_{sc} for the perovskite cell is smaller than the decrease for the silicon cell. This discrepancy is due to increased recombination in the thicker perovskite layer, which creates a larger difference between the absorbed current density (J_{abs}) and the J_{sc}, where J_{abs} is defined as

$$J_{abs} = q \cdot \int A(\lambda) \cdot \phi(\lambda) d\lambda,$$

where $A(\lambda)$ is the spectral absorptance, and $\phi(\lambda)$ is the spectral photon flux.

Fig. 4 shows the difference between J_{abs} and J_{sc} for different thicknesses, revealing that the J_{sc} saturates at around 600 nm. This is also experimentally shown in [26], where the J_{sc} even decreases for larger thicknesses. For smaller thicknesses, J_{sc} is slightly larger than J_{abs}. This is because photons absorbed in the HTL and ETL (indicated with light blue) of the perovskite have a small contribution to the current generation, making J_{sc} larger than only the absorbed current in the perovskite.

3.2. The different operating conditions

The optimization is done for four geographical locations to determine if different climates, corresponding to different spectral irradiance conditions and temperatures, require different optimal perovskite cells. The locations are chosen such that they represent a different climate according to the Köppen-Geiger-Photovoltaics (KGPV) classification [45,46]. The selected locations are Delft (the Netherlands), Shanghai (China), Lagos (Nigeria), and Lisbon (Portugal) The most important characteristics are shown in Table 1. All modules are 0.5 m above the ground, and the distance between the modules is 1 m in the east–west and 8 m in the north–south direction.

The reflectivity of the ground material below the module is an important aspect of system design because bifacial modules receive irradiance reflected from the ground on their rear side as well. To understand how ground material impacts optimal parameters, we simulated three different types in each location: dry soil, grass, and a white Medium Density Fibreboard (MDF). The spectral reflectivity of these materials is shown in Fig. 5. Also the irradiance weighted albedo (R_a) is indicated in the figure. For R_a, we use the equation defined by C. A. Gueymard [47] (defined in Appendix A).

4. Results

Simulations with the PVMD Toolbox are used to identify the optimal perovskite for the different operating conditions. For each situation, the optimal perovskite cell is found by varying the thickness and bandgap energy of the perovskite. The simulation steps of the bandgap energy and thickness are 0.01 eV and 50 nm, respectively. First, validation and the different Cell-to-Module losses are discussed and quantified to explain the difference between the performance at cell level and the performance at module level. Then, the difference in spectral irradiation among the different situations is analyzed, as this is considered to be the most important characteristic determining the optimal cell.

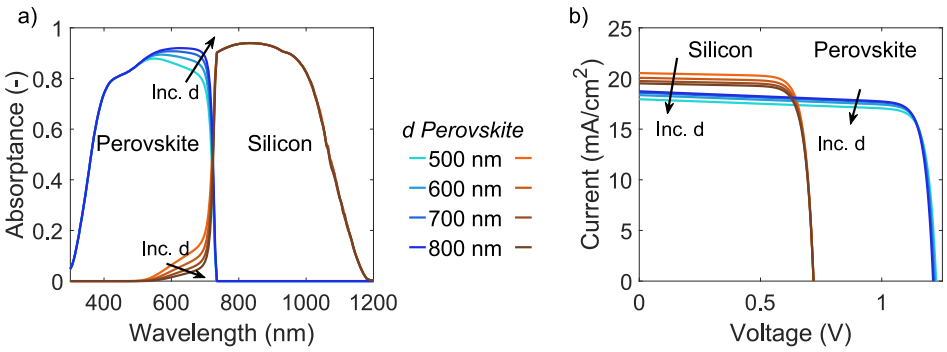

Fig. 3. The effect of changing the perovskite layer thickness on the absorptance in perovskite and silicon (a) and the JV curves of the subcells (b). For both figures, a bandgap energy of 1.67 eV is used.

Table 1
The most important characteristics of the selected locations. The ambient temperature is weighted with the global horizontal irradiance, which is defined in Appendix A. The selected KGPV classifications are temperate-low irradiation (DL), temperate-medium irradiation (DM), tropical-high irradiation (AH), and temperate-high irradiation (DH).

Location	Annual global horizontal irradiation [kW h m^{-2}]	Weighted average ambient temperature [°C]	KGPV	Optimal module tilt [°]
Delft	1018	16.2	DL	38
Shanghai	1271	21.7	DM	23
Lagos	1642	29.4	AH	8
Lisbon	1758	20.6	DH	33

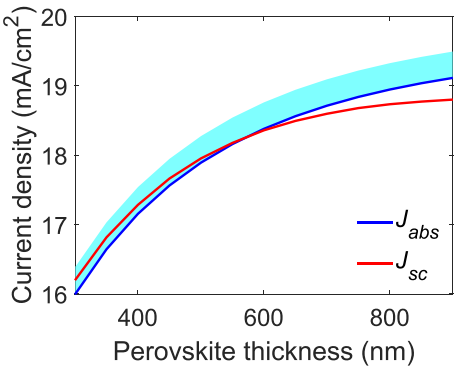

Fig. 4. A comparison of the absorbed photocurrent density and the short circuit density for the perovskite cell with increasing thickness. The absorption in the HTL and ETL (indicated in blue) can contribute to the short circuit current, explaining the larger J_{sc} for small thicknesses. The larger difference between J_{abs} and J_{sc} is due to increasing recombination for larger thicknesses.

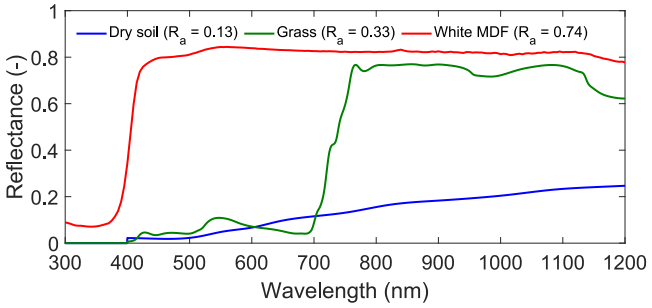

Fig. 5. The reflectance of the simulated ground materials. R_a represents the irradiance weighted albedo.

This is followed by the optimization of the perovskite cell, where the trends in the loss mechanisms are used to explain the obtained results. Finally, the bifacial perovskite/silicon tandem modules are compared with bifacial c-Si modules and monofacial perovskite/silicon modules to assess the gain in energy yield.

4.1. Validation and Cell-to-Module losses

It is important to note that the validation was conducted on a lab-scale cell with an efficiency of 32.5%. The simulated cell efficiency is slightly higher at 32.7% (Fig. 6) compared to the reference efficiency of 32.5%, but this deviation is within measurement accuracy. It should be realized that this validation is performed for STC, meaning that the temperature- and irradiance-dependencies were not included. However, the PVMD Toolbox has been validated for the outdoor performance of c-Si modules [29], validating the thermal and irradiance models.

When the cells are integrated into a module, various Cell-to-Module (CTM) losses occur, reducing the overall efficiency. Fig. 6 illustrates the loss analysis for both the lab-scale cell and the bifacial module under STC.

Several losses are introduced due to cell interconnection, such as metal shading losses (0.5%) and interconnection losses (0.2%). Encapsulation further contributes to losses, with reflection losses increasing from 1.6% to 2.9% and parasitic absorption from 1.4% to 2.4%. Additionally, the spacing between cells introduces a non-active area, resulting in an additional 2.8% loss. These factors reduce the efficiency from 32.7% at the cell level to 28.2% at the module level, meaning that the CTM losses are 4.5%. This is much larger than the CTM losses for a c-Si module shown in Appendix B, which are only 3.5%. Due to the lower fundamental losses for tandem devices (50% compared to 66% for c-Si), the other losses have a greater impact. Then, when these other losses increase due to the module integration, this has a larger impact on the efficiency, explaining why the CTM losses are larger for tandem devices.

4.2. The irradiation

As the received irradiance largely influences the optimal perovskite cell, it is crucial to understand how this changes for the different operating conditions. Fig. 7 shows the received irradiance on the front and rear side of the PV module in the different locations. Also, the effective albedo (R_a^*) of the different situations is shown, which is defined as the

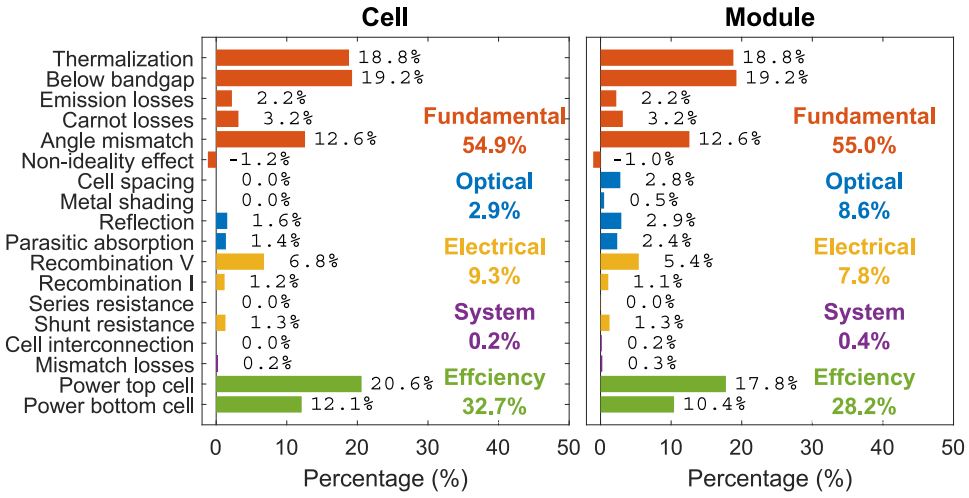

Fig. 6. The loss analysis of the lab-scale cell (a) and the bifacial module (b) under STC conditions. It should be noted that only the front irradiance is considered to be consistent with the validation measurement.

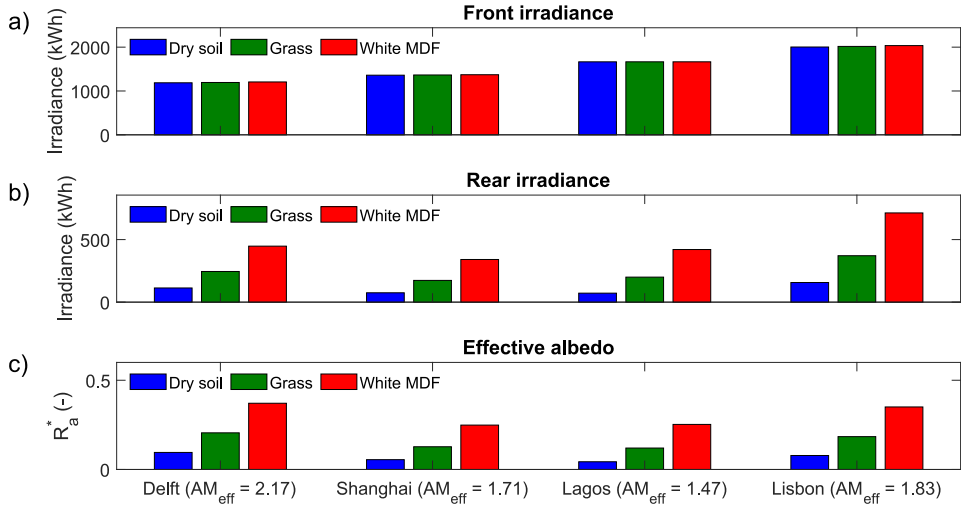

Fig. 7. The received front (a) and rear (b) irradiance for the locations with the different ground materials. Also the effective albedo (c) is displayed for all situations. AM_{eff} stands for the effective air mass and is computed according to the definition in Appendix A.

ratio of the received irradiance on the rear side compared to that of the front side. As explained by Jahangir et al. [22], this parameter can vary significantly with respect to R_a. This is because R_a^* also depends on the module geometry and the surroundings. Additionally, it is possible that diffuse irradiance can reach the rear side of the module without requiring a reflection via the ground, contributing to the received irradiance on the rear side. This will also cause a difference between R_a and R_a^*.

As can be seen from Fig. 7, the ground material hardly affects the received irradiance on the front side but plays a significant role in the rear irradiance. Lagos and Lisbon receive the most front irradiance, as these locations experience the largest annual global horizontal irradiation (Table 1). Delft and Lisbon have the largest effective albedo for all ground materials, as the tilt of the modules is largest at these locations. This larger tilt creates a larger sky view factor for the rear side of the module, leading to more rear irradiance and a larger effective albedo. Fig. 7 also shows the effective air mass (AM_{eff}) (defined in Appendix A) on the x-axis labels for each location. Locations near the equator (Lagos) have a smaller air mass than locations at a larger latitude (Delft), indicating that the spectrum in these locations has a blue-shift.

4.3. Optimal perovskite E_g and d

We use the PVMD Toolbox to calculate the energy yield of the different tandem designs under the various operating conditions. To compare the different locations, we use the annual module efficiency (η_{mod}) as metric, which is defined as

$$\eta_{mod} = \frac{\int P_{out}(t)dt}{A_{mod} \cdot \int \cdot Irr_{in}(t)dt}, \tag{1}$$

where $P_{out}(t)$ and Irr_{in} are the generated electricity and incoming irradiance from the front and rear side, respectively, at time t, and A_{mod} is the area of the module. Fig. 8 shows η_{mod} of all combinations of bandgap energy and thickness of the perovskite layer and highlights the optimal one. The thickness maximizing the efficiency ranges from 650–750 nm under all conditions. This optimal thickness is linked to the trend observed in Fig. 4, where J_{abs} is compared with J_{sc} for different thicknesses. Since J_{sc} starts to saturate around 700 nm, there is no gain of increasing the perovskite thickness further, explaining the optimal thickness range.

The optimal bandgap energy is in the range of 1.61–1.65 eV, which is in the same range as observed in literature [16,18–20] and only changes slightly for different ground materials. Additionally, Delft and Lisbon have a smaller optimal bandgap energy than Shanghai and

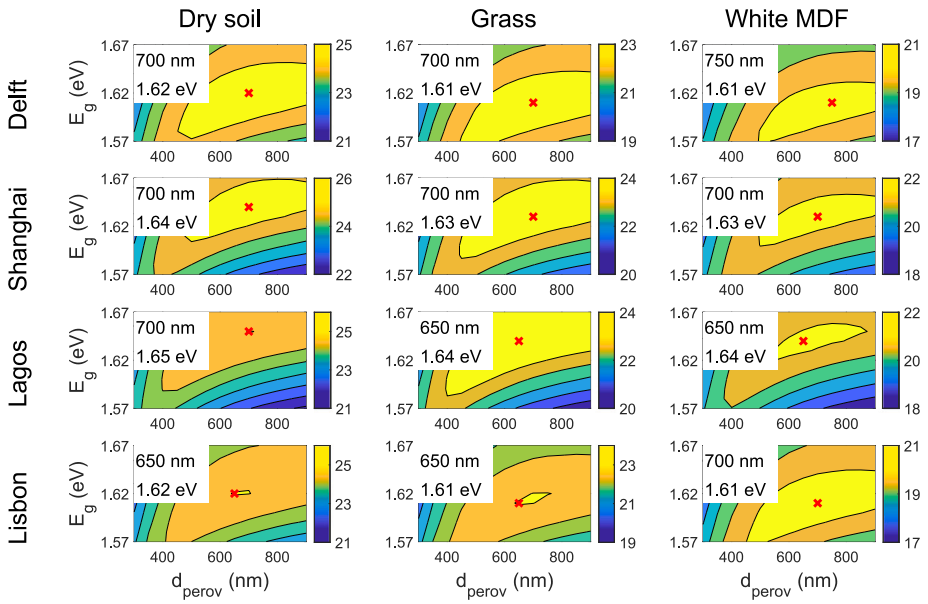

Fig. 8. η_{mod} for all combinations of d_{perov} and E_g under the different operating conditions (i.e. location and ground reflectivity). The optimal combination is indicated with the cross, and its values are shown in the top left corner.

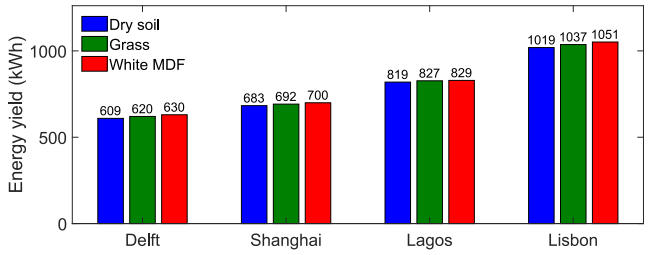

Fig. 9. The energy yield of the bifacial modules endowed with optimized tandem solar cells under different conditions.

Lagos. This can be explained by the larger effective air mass for these locations (shown in Fig. 7). A larger air mass corresponds to a more red-shifted light spectrum, meaning that fewer photons are available in the perovskite absorption range. To compensate, the perovskite bandgap energy should be lower. A more detailed discussion on the optimal thickness and bandgap energy will be provided later in this section.

To analyze the effect of bifaciality on the optimal perovskite thickness and bandgap energy, the optimization has also been performed for monofacial devices. As shown in Appendix C, the optimal bandgap energy is approximately 0.2 eV lower for the bifacial modules.

The energy yields of the optimized tandem modules are shown in Fig. 9. Lisbon has the highest energy yield since it has the largest annual global horizontal irradiation combined with a relatively low ambient temperature (Table 1). Surprisingly, the ground material hardly affects the energy yield, even though the white MDF provides significantly more irradiance on the rear side. The causes of this result will be explained later in the section.

4.4. The energy losses

To understand why the values shown in Fig. 8 are optimal, studying the different losses within a PV module can be helpful. We use the methodology outlined in our previous work [24] to quantify all losses. In the main text, we will only show the analysis of Delft, as the trends are similar for all locations. The results for the other locations can be found in Appendix D. Fig. 10 shows the loss distributions in Delft for the different ground materials. For each situation, the optimal perovskite design is used.

The situation with dry soil as ground material provides the highest efficiency (24.8%), and the efficiency is the lowest in the situation with the white MDF as ground material (20.2%). This appears to be significantly lower than the STC efficiency of 28.2% (Fig. 6). This is due to the fact that the irradiance received on the rear side cannot be converted as efficiently as the irradiance on the front side. Whereas front-side irradiance is absorbed in both perovskite and c-Si, rear-side irradiance is only converted in the c-Si bottom cell, a device with lower efficiency and more thermalization losses. This also explains why the simulation with the white MDF as ground material has the highest energy yield (Fig. 9), but the lowest efficiency. Due to the larger rear irradiance, it can generate more electricity, but the overall efficiency is lower as the fraction of rear irradiance is more significant. As shown in Fig. 10, the simulation with the white MDF reflector, has a significant increase in thermalization losses compared to the dry soil simulation. This effect, however, can be lowered by improving the efficiency of the bottom cell.

Another loss that varies greatly among the different materials is the reflection loss. The light reflectance increases for a larger angle of incidence. Since light at the rear side tends to come at more oblique angles than the front side, the reflection losses increase for situations with more rear-side irradiation.

Finally, the mismatch losses are significantly larger for the grass and white MDF settings. This is caused by the additional rear irradiance received with those ground materials. One would expect that the increased mismatch losses can be reduced by changing the bandgap energy or the thickness. However, Fig. 11 shows that the combination of perovskite bandgap and thickness that maximize the energy yield (indicated by the red cross) is not the same combination that minimizes the mismatch losses (indicated by the green cross). For all ground materials, the mismatch losses would be lower for a smaller bandgap energy or thickness. Nevertheless, changing the bandgap energy or thickness would increase other losses, decreasing the overall efficiency. This is discussed in more detail in the next sections.

4.4.1. Changing the perovskite bandgap energy

As shown in Fig. 11, the mismatch losses could be reduced by lowering the bandgap energy. However, this would increase the thermalization losses. As thermalization losses depend on the difference between the energy of the photon and the bandgap energy, reducing

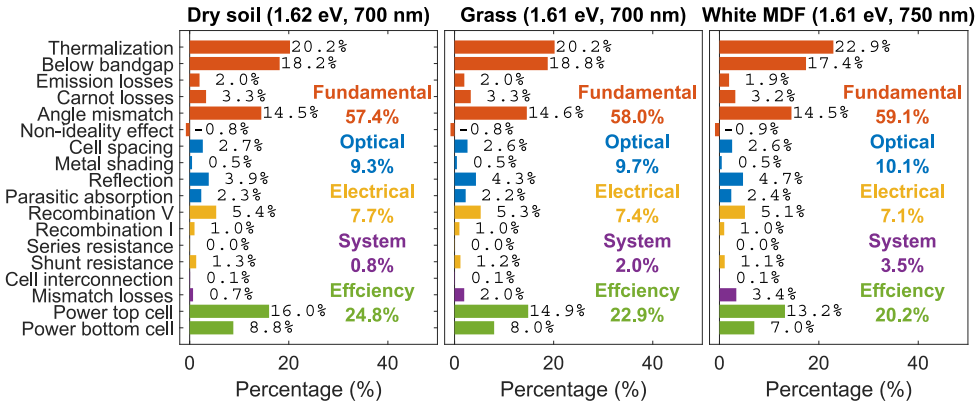

Fig. 10. The loss distribution in Delft for the different ground materials. The optimal bandgap energy and thickness of the perovskite are shown for each situation.

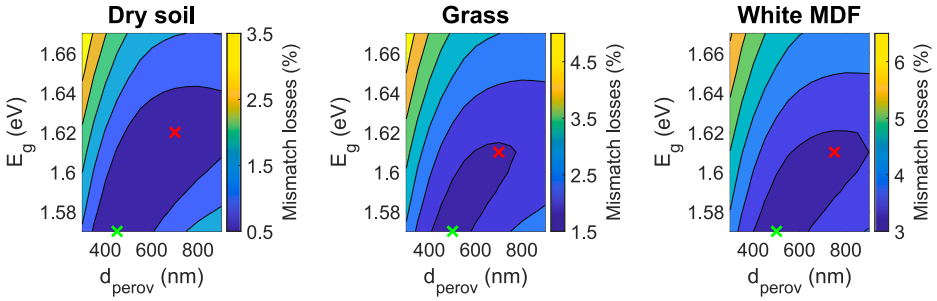

Fig. 11. The mismatch losses for the different perovskite cells in Delft. The optimal combination of bandgap energy and thickness for maximizing energy yield (indicated with the red cross) does not minimize the mismatch losses (the green cross indicates the combination minimizing the mismatch losses).

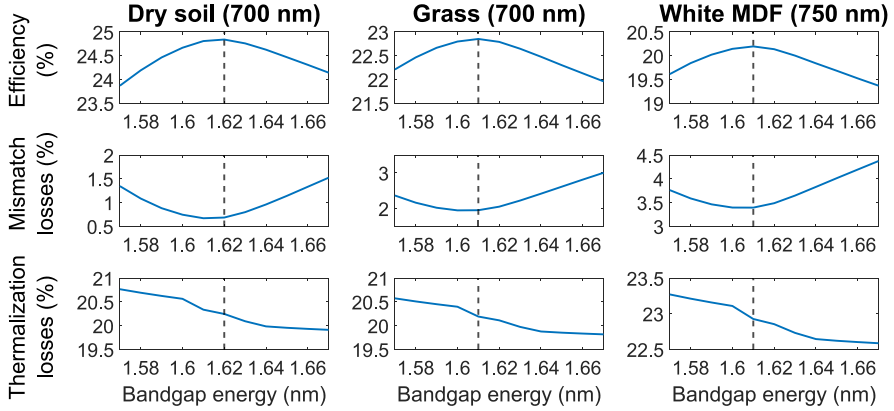

Fig. 12. The annual module efficiency as well as mismatch, and thermalization losses for different bandgap energies. The optimal bandgap energy is indicated with a dashed line. Lowering the bandgap energy will increase the thermalization losses, meaning the mismatch losses cannot be minimized.

the bandgap energy will affect the thermalization losses. Fig. 12 shows how the efficiency, mismatch, and thermalization losses change for various bandgap energies. The thermalization losses increase for a lower bandgap energy, which is in agreement with literature [48]. This means that the mismatch losses cannot be fully minimized without reducing η_{mod}, showing that the optimal bandgap energy is mostly a trade-off between the mismatch and thermalization losses. Our results show that the ideal bandgap is about 0.01 eV higher than the one that minimizes mismatch losses as this reduces thermalization losses more significantly.

4.4.2. *Changing the perovskite thickness*

Another method for reducing the mismatch losses is to change the perovskite thickness. However, the thermalization losses do not only depend on the bandgap energy but also on the thickness. When reducing the thickness of the perovskite, its absorption reduces as well, meaning that more high-energy photons will be transmitted and absorbed in the silicon layer. As silicon has a smaller bandgap energy, the thermalization losses increase for these photons. This effect is also described by [49] and is included in the non-ideality gain [24]. Fig. 13 shows how the efficiency, mismatch losses, and non-ideality gain are related to the perovskite thickness. A smaller thickness will reduce the non-ideality gain, meaning the thermalization losses have increased. Therefore, the optimization of the perovskite thickness is also a trade-off between the thermalization and mismatch losses. This indicates that the device with the best current matching may not yield the highest energy output but, instead, a thicker top cell is generally more favorable.

The module with white MDF as the ground reflector has an optimal perovskite thickness of 750 nm, slightly higher than the 700 nm optimal

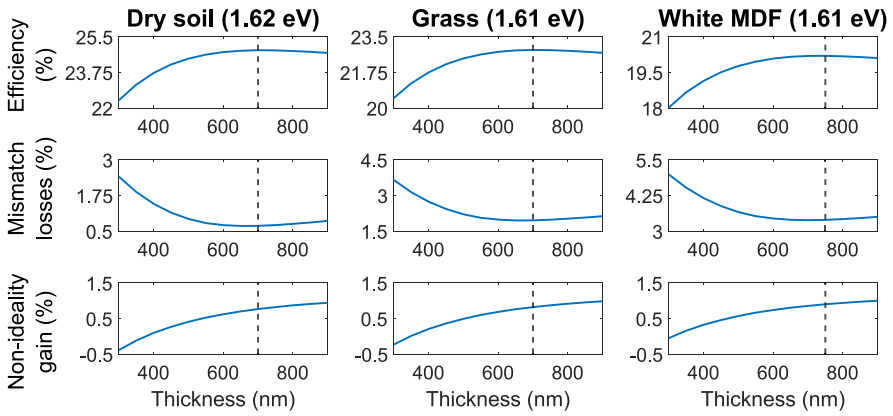

Fig. 13. The efficiency, mismatch losses, and non-ideality gain for different perovskite absorber thicknesses. The optimal thickness is indicated with a dashed line. Lowering the thickness will lower the non-ideality gain, meaning the mismatch losses cannot be minimized.

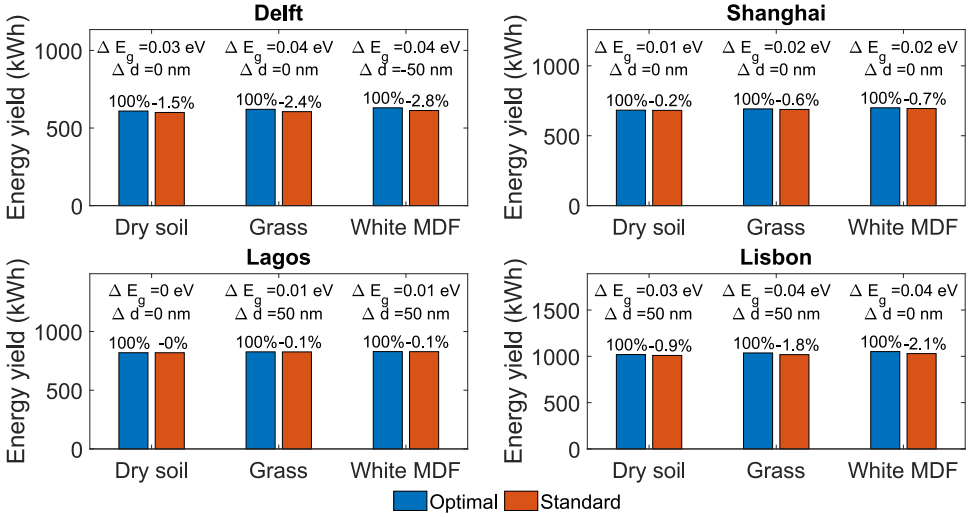

Fig. 14. The deviation between the optimized and standard bifacial tandem modules. The used perovskite bandgap energy and thickness are 1.65 eV and 700 nm. Also, ΔE_g and Δ d are shown for all operating conditions.

thickness for modules with grass or dry soil backgrounds. However, this apparent significant difference is influenced by the 50 nm step size used in the analysis and the very similar efficiencies observed, indicating a range of optimal thicknesses rather than a precise value. The increased reflected irradiance from the white MDF background enhances absorption in the bottom cell, creating a mismatch between the top and bottom cells. A greater perovskite thickness helps compensate for this mismatch, resulting in a slightly higher efficiency for the white MDF scenario.

4.5. Deviation between optimized and standard modules

Fig. 8 shows that the optimal bandgap energy and thickness are relatively consistent across different locations. However, standardizing the production of PV modules could benefit the industry as the throughput can be increased [50]. As a result, it may be more economically feasible to use PV modules with a standard bandgap energy and thickness, rather than optimizing these parameters for specific locations.

Fig. 14 illustrates the impact on energy yield when using average optimal values for bandgap energy (1.65 eV) and thickness (700 nm) in bifacial modules, instead of location-specific optimized values. Also, the differences in bandgap energy (ΔE_g) and thickness (Δd) between the standard and optimal simulation are indicated in the figure. It can be seen that the deviation is correlated with ΔE_g, indicating that this has a larger impact than Δd.

In all cases, the energy yield loss is less than 3%. However, further economic analysis is needed to determine whether producing standardized modules or condition-specific optimized ones is more cost-effective.

4.6. Comparison with monofacial and single-junction modules

Finally, the performance of the bifacial tandem module is compared with that of modules based on other solar cell architectures, including monofacial and bifacial single-junction devices, as well as optimized monofacial and bifacial tandem devices. The silicon heterojunction (SHJ) monofacial and SHJ bifacial modules are designed using the bottom part of the tandem cell depicted in Fig. 1, with front texturing added to make the modules more representative of real PV systems.

Fig. 15 shows the energy yield of the bifacial SHJ and tandem modules. The figure also quantifies the gain of turning monofacial tandem modules into bifacial ones (Δ_{bif}), and the gain of turning bifacial SHJ modules into bifacial tandem modules (Δ_{tan}).

Under all conditions, the bifacial tandem device consistently achieves the highest performance. Their energy yield is always more than 25% larger compared to bifacial SHJ modules (Δ_{tan}), and can be up to 5% higher than that of monofacial tandem devices (Δ_{bif}). The difference between the monofacial and bifacial tandems is the smallest in Lagos. This is due to the relatively low rear irradiance that is received at this location (Fig. 7) resulting from a low module tilt of just 8°. In all

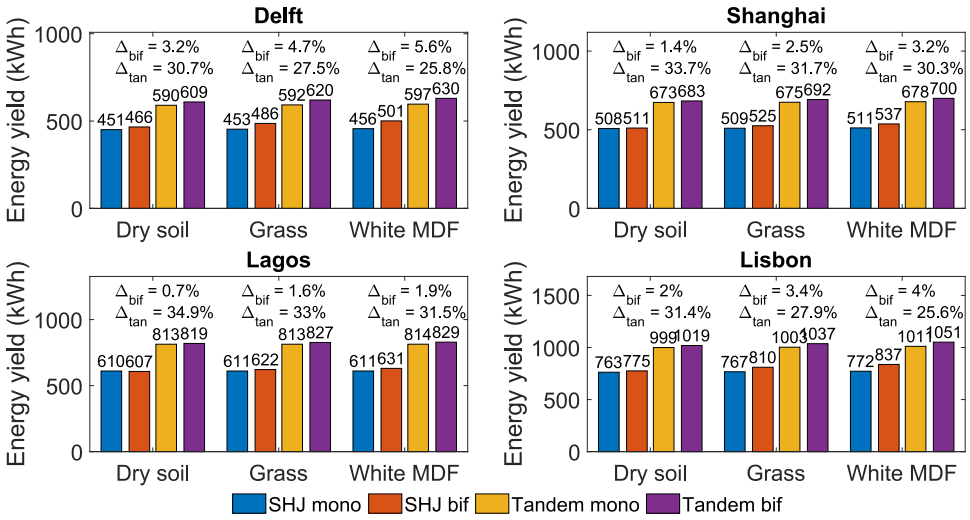

Fig. 15. A comparison in energy yield between the different modules. For the tandem devices, the optimum perovskite cell is used. Δ_{bif} indicates the gain of making a monofacial tandem module bifacial, and Δ_{tan} indicates the gain of turning a bifacial SHJ module into a bifacial tandem module.

locations, the gain of the bifacial tandem over the monofacial tandem increases with more reflective ground materials.

It should be realized that the bifacial gain also depends largely on the module geometry, which is kept constant in this study. Future research is needed to quantify the effect of module tilt, module height, and the distance between the modules on the bifacial gain and energy yield.

5. Conclusion

In this work, we have presented the optimization of the perovskite cell for a bifacial perovskite/silicon module. Our analysis includes aspects that had thus far not been fully discussed and included in literature. Instead of only optimizing the bandgap energy of the perovskite, we also analyzed the impact of different thicknesses on the energy performance. The optimal perovskite bandgap energy and thickness were found for four locations with three different ground materials. The optimal bandgap energy lies in the range of 1.61–1.65 eV for all locations, and the optimal thickness is 650–750 nm. The bandgap energy is slightly lower for locations with a higher air mass, due to the red shift in the spectrum. The energy yield varies greatly for different locations but has a lower dependency on the ground material. This is due to the rear side irradiance is converted less efficiently than the front side irradiance, due to thermalization and reflection losses.

The optimal bandgap energy and thickness is mostly a trade-off between the mismatch and thermalization losses. Although lowering both the bandgap energy and the thickness will decrease the mismatch losses, it will also increase the thermalization losses. This leads to the optimal combination of bandgap energy and thickness, which does not minimize mismatch losses.

Although the optimal perovskite cell is slightly different for all conditions, the loss in energy yield when using a standardized module is smaller than 3% for all situations. This can be used for further economical analysis to analyze what is the most cost-effective tandem design.

Finally, the energy yield of bifacial tandems is compared with bifacial SHJ and monofacial tandem modules. For all conditions, the bifacial tandem module has the highest performance, having a ≥25% and 5% increase in energy yield compared to bifacial SHJ and monofacial tandems respectively. This shows that combining multi-junction solar cells with bifacial modules can lead to high-performance PV systems, further increasing the energy yield per unit area.

CRediT authorship contribution statement

Youri Blom: Writing – original draft, Visualization, Software, Methodology, Investigation. **Malte Ruben Vogt:** Writing – review & editing, Supervision. **Olindo Isabella:** Writing – review & editing, Supervision. **Rudi Santbergen:** Writing – review & editing, Supervision, Methodology.

Declaration of Generative AI and AI-assisted technologies in the writing process

During the preparation of this work the author(s) used ChatGPT in order to paraphrase sentences and improve the language and readability. After using this tool/service, the author(s) reviewed and edited the content as needed and take(s) full responsibility for the content of the publication

Declaration of competing interest

The authors declare that they have no known competing financial interests or personal relationships that could have appeared to influence the work reported in this paper.

Appendix A. Mathematical definitions

Different metrics are used in the main work to either characterize the operating conditions or the results. This section provides the mathematical definitions of these metrics.

The weighted average ambient temperature (T^*_{amb}) is used to characterize the temperature profile of the locations. Since periods of high irradiance contribute more to annual energy yield, weighting the ambient temperature (T_{amb}) with the irradiance is more representative than simply the average T_{amb}. T^*_{amb} is calculated with

$$T^*_{amb} = \frac{\sum T_{amb,t} \cdot \mathrm{GHI}_t}{\sum \mathrm{GHI}_t}, \tag{A.1}$$

where $T_{amb,t}$ and GHI_t are the ambient temperature and global horizontal irradiance at time t, respectively.

To characterize the reflectivity of ground materials, we use the irradiance-weighted albedo (R_a) as defined by C. A. Gueymard [47], written as

$$R_a = \frac{\int R_\lambda(\lambda) \cdot I_{\lambda,AM1.5}(\lambda) d\lambda}{\int I_{\lambda,AM1.5}(\lambda) d\lambda}, \tag{A.2}$$

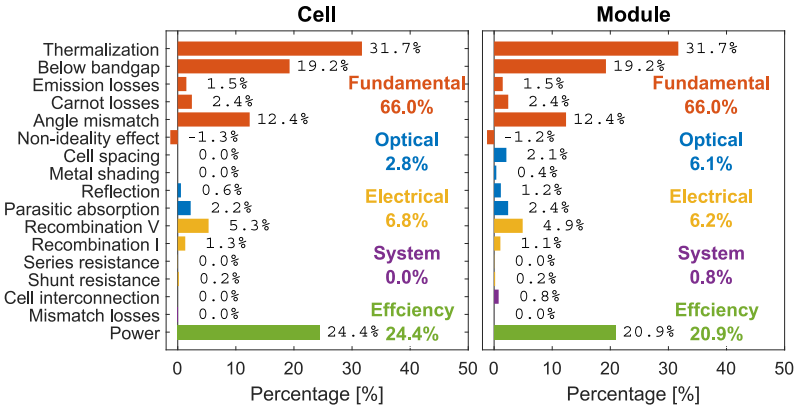

Fig. B.1. The loss analysis of the lab-scale SHJ cell (a) and the bifacial module (b) under STC conditions. It should be noted that only front irradiance is considered to be consistent with the validation measurement.

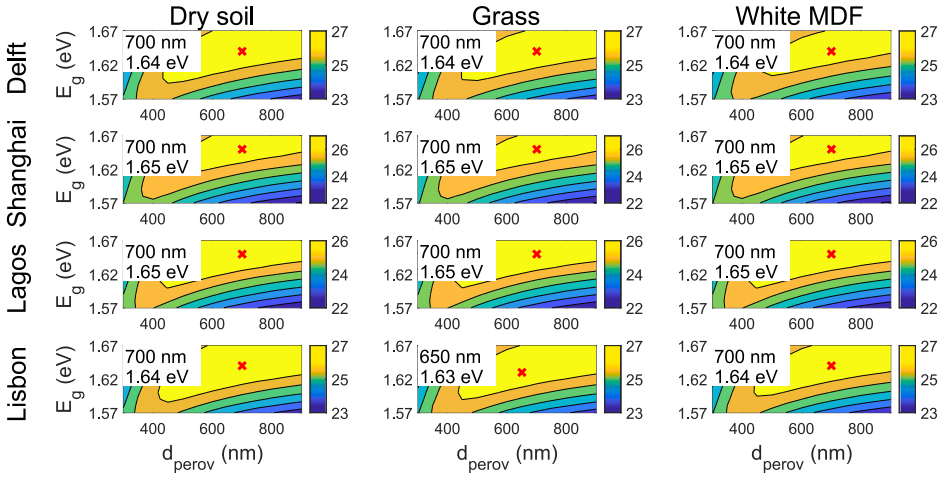

Fig. C.1. The optimal perovskite cell under the different operating conditions for monofacial devices. MDF stands for Medium Density Fibreboard.

where $R_\lambda(\lambda)$ is the reflectance, and $I_{\lambda,AM1.5}(\lambda)$ is the spectral irradiance of the AM1.5 spectrum.

The spectral irradiance received by the PV module depends heavily on the air mass (AM) of each location. As mentioned before, periods with high irradiance are more relevant, meaning that weighted the AM with the irradiance provides a better characterization of the location. The effective air mass (AM_{eff}) is therefore defined as

$$T^*_{amb} = \frac{\sum \mathrm{AM}_t \cdot \mathrm{GHI}_t}{\sum \mathrm{GHI}_t}. \tag{A.3}$$

Appendix B. Cell-to-Module losses for SHJ

In the main text, it was shown that the Cell-to-Module (CTM) losses of the tandem module are 4.5%. Fig. B.1 shows that the CTM losses for a SHJ module are 3.5%. This decrease in efficiency arise from an increase in cell spacing losses (from 0% to 2.1%), metal shading losses (from 0% to 0.4%), and reflection losses (from 0.6% to 1.2%).

Appendix C. Optimization monofacial tandem module

The optimization of the perovskite bandgap energy and thickness is also performed for monofacial modules. Fig. C.1 shows the annual module efficiency of the monofacial devices under operating conditions.

It can be seen that the optimal bandgap energy and thickness are 1.64–1.65 eV and 700 nm, respectively, and do not vary significantly. The optimal bandgap energy is slightly larger in Shanghai and Lagos due to their lower air mass. Also, it can be seen that there is no effect of the ground material on the optimal values, as these monofacial devices cannot receive any rear irradiance.

Appendix D. Results different climates

Fig. 10 shows the loss distribution of the optimal modules simulated in Delft. The same analysis is also performed for the Shanghai, Lagos, and Lisbon, which are shown in Figs. D.1, D.2, and D.3 respectively. The same trends can be observed as the ones discussed in the main text.

Appendix E. Supplementary data

Supplementary material related to this article can be found online at https://doi.org/10.1016/j.solmat.2025.113431.

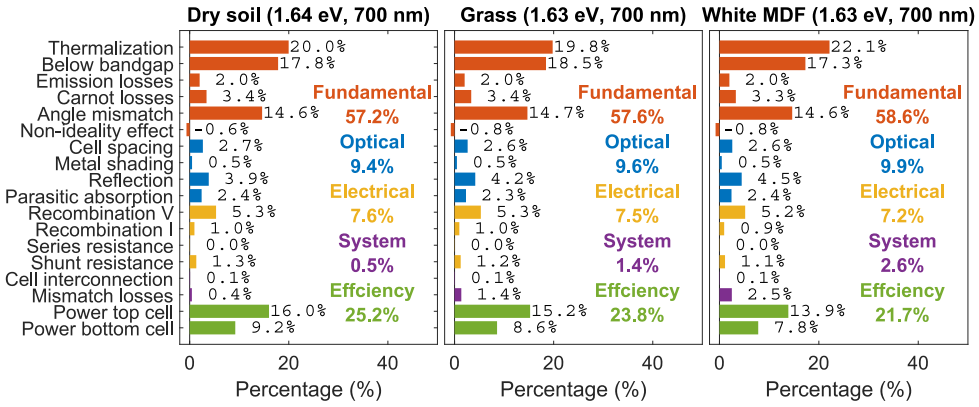

Fig. D.1. The loss distribution in Shanghai for the different ground materials. The optimal bandgap energy and thickness of the perovskite are shown for each situation.

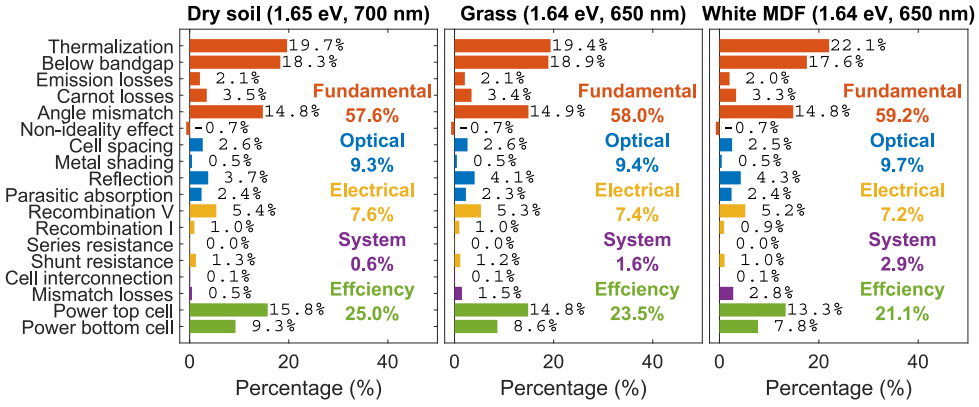

Fig. D.2. The loss distribution in Lagos for the different ground materials. The optimal bandgap energy and thickness of the perovskite are shown for each situation.

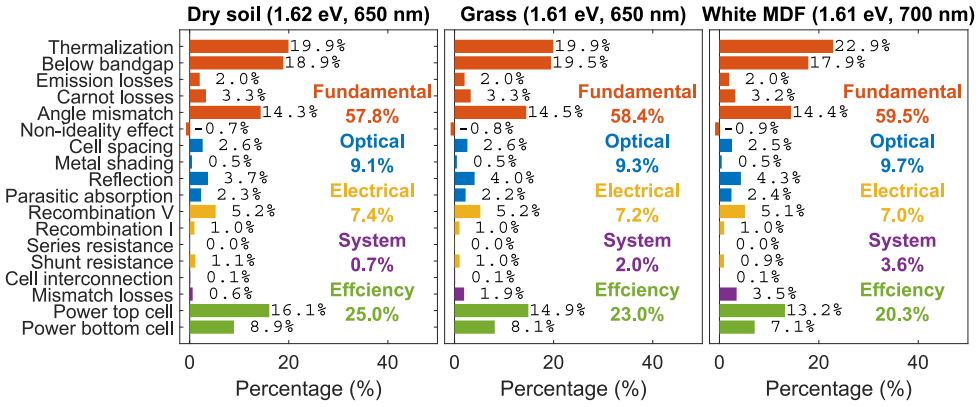

Fig. D.3. The loss distribution in Lisbon for the different ground materials. The optimal bandgap energy and thickness of the perovskite are shown for each situation.

Data availability

We have included the data underlying Figure 8 supporting information. Any other data is available upon request.

References

[1] VDMA, International technology roadmap for photovoltaics (ITRPV), 2024.

[2] LONGi sets new world-record for silicon solar cell efficiency, launching 2nd generation ultra-efficient BC-based module, 2024, URL https://www.longi.com/en/news/longi-hi-mo9-bc-world-record/.

[3] A. Richter, M. Hermle, S.W. Glunz, Reassessment of the limiting efficiency for crystalline silicon solar cells, IEEE J. Photovolt. 3 (4) (2013) 1184–1191, http://dx.doi.org/10.1109/JPHOTOV.2013.2270351.

[4] S. Schafer, R. Brendel, Accurate calculation of the absorptance enhances efficiency limit of crystalline silicon solar cells with lambertian light trapping, IEEE J. Photovolt. 8 (4) (2018) 1156–1158, http://dx.doi.org/10.1109/JPHOTOV.2018.2824024.

[5] A.D. Vos, Detailed balance limit of the efficiency of tandem solar cells, J. Phys. D: Appl. Phys. 13 (5) (1980) 839–846, http://dx.doi.org/10.1088/0022-3727/13/5/018.

[6] H. Zhang, X. Ji, H. Yao, Q. Fan, B. Yu, J. Li, Review on efficiency improvement effort of perovskite solar cell, Sol. Energy 233 (2022) 421–434, http://dx.doi.org/10.1016/j.solener.2022.01.060.

[7] J.J. Yoo, G. Seo, M.R. Chua, T.G. Park, Y. Lu, F. Rotermund, Y.-K. Kim, C.S. Moon, N.J. Jeon, J.-P. Correa-Baena, V. Bulović, S.S. Shin, M.G. Bawendi, J. Seo, Efficient perovskite solar cells via improved carrier management, Nature 590 (7847) (2021) 587–593, http://dx.doi.org/10.1038/s41586-021-03285-w.

[8] S. Manzoor, J. Häusele, K.A. Bush, A.F. Palmstrom, J. Carpenter, Z.J. Yu, S.F. Bent, M.D. Mcgehee, Z.C. Holman, Optical modeling of wide-bandgap perovskite

and perovskite/silicon tandem solar cells using complex refractive indices for arbitrary-bandgap perovskite absorbers, Opt. Express 26 (21) (2018) 27441, http://dx.doi.org/10.1364/OE.26.027441.
[9] M.A. Green, E.D. Dunlop, M. Yoshita, N. Kopidakis, K. Bothe, G. Siefer, X. Hao, Solar cell efficiency tables (version 62), Prog. Photovolt., Res. Appl. 31 (7) (2023) 651–663, http://dx.doi.org/10.1002/pip.3726.
[10] S. Mariotti, E. Köhnen, F. Scheler, K. Sveinbjörnsson, L. Zimmermann, M. Piot, F. Yang, B. Li, J. Warby, A. Musiienko, D. Menzel, F. Lang, S. Keßler, I. Levine, D. Mantione, A. Al-Ashouri, M.S. Härtel, K. Xu, A. Cruz, J. Kurpiers, P. Wagner, H. Köbler, J. Li, A. Magomedov, D. Mecerreyes, E. Unger, A. Abate, M. Stolterfoht, B. Stannowski, R. Schlatmann, L. Korte, S. Albrecht, Interface engineering for high-performance, triple-halide perovskite–silicon tandem solar cells, Science 381 (6653) (2023) 63–69, http://dx.doi.org/10.1126/science.adf5872.
[11] KAUST team sets world record for tandem solar cell efficiency, 2023, URL https://www.kaust.edu.sa/en/news/kaust-team-sets-world-record-for-tandem-solar-cell-efficiency.
[12] R. Guerrero-Lemus, R. Vega, T. Kim, A. Kimm, L. Shephard, Bifacial solar photovoltaics – a technology review, Renew. Sustain. Energy Rev. 60 (2016) 1533–1549, http://dx.doi.org/10.1016/j.rser.2016.03.041.
[13] R. Hezel, Novel applications of bifacial solar cells, Prog. Photovolt., Res. Appl. 11 (8) (2003) 549–556, http://dx.doi.org/10.1002/pip.510.
[14] A. Onno, N. Rodkey, A. Asgharzadeh, S. Manzoor, Z.J. Yu, F. Toor, Z.C. Holman, Predicted power output of silicon-based bifacial tandem photovoltaic systems, Joule 4 (3) (2020) 580–596, http://dx.doi.org/10.1016/j.joule.2019.12.017.
[15] M.T. Patel, R. Asadpour, J. Bin Jahangir, M. Ryyan Khan, M.A. Alam, Current-matching erases the anticipated performance gain of next-generation two-terminal Perovskite-Si tandem solar farms, Appl. Energy 329 (2023) 120175, http://dx.doi.org/10.1016/j.apenergy.2022.120175.
[16] H. Hao, S.-T. Zhang, K. Wang, P. Yang, J. Wang, L. Yang, L. Lu, D. Li, Energy yield prediction of bifacial perovskite/silicon tandem photovoltaic modules, Sol. RRL 7 (15) (2023) http://dx.doi.org/10.1002/solr.202300218.
[17] L. Xu, F. Xu, J. Liu, X. Zhang, A.S. Subbiah, S. De Wolf, Bandgap optimization for bifacial tandem solar cells, ACS Energy Lett. (2023) 3114–3121, http://dx.doi.org/10.1021/acsenergylett.3c01014.
[18] M. De Bastiani, A.J. Mirabelli, Y. Hou, F. Gota, E. Aydin, T.G. Allen, J. Troughton, A.S. Subbiah, F.H. Isikgor, J. Liu, L. Xu, B. Chen, E. Van Kerschaver, D. Baran, B. Fraboni, M.F. Salvador, U.W. Paetzold, E.H. Sargent, S. De Wolf, Efficient bifacial monolithic perovskite/silicon tandem solar cells via bandgap engineering, Nat. Energy 6 (2) (2021) 167–175, http://dx.doi.org/10.1038/s41560-020-00756-8.
[19] K. Jäger, P. Tillmann, E.A. Katz, C. Becker, Perovskite/silicon tandem solar cells: Effect of luminescent coupling and bifaciality, Sol. RRL 5 (3) (2021) 2000628, http://dx.doi.org/10.1002/solr.202000628.
[20] J. Lehr, M. Langenhorst, R. Schmager, F. Gota, S. Kirner, U. Lemmer, B.S. Richards, C. Case, U.W. Paetzold, Energy yield of bifacial textured perovskite/silicon tandem photovoltaic modules, Sol. Energy Mater. Sol. Cells 208 (2020) 110367, http://dx.doi.org/10.1016/j.solmat.2019.110367.
[21] M. Singh, R. Santbergen, I. Syifai, A. Weeber, M. Zeman, O. Isabella, Comparing optical performance of a wide range of perovskite/silicon tandem architectures under real-world conditions, Nanophotonics 10 (8) (2021) 2043–2057, http://dx.doi.org/10.1515/nanoph-2020-0643.
[22] J.B. Jahangir, M.T. Patel, R. Asadpour, M.R. Khan, M.A. Alam, Planet-scale energy yield potential of next-generation bifacial, multiterminal, perovskite-silicon tandem solar farms, IEEE J. Photovolt. (2024) 1–9, http://dx.doi.org/10.1109/JPHOTOV.2023.3340602.
[23] F. Gota, S.X. An, H. Hu, B. Abdollahi Nejand, U.W. Paetzold, Energy yield modeling of bifacial all-perovskite two-terminal tandem photovoltaics, Adv. Opt. Mater. (2022) 2201691, http://dx.doi.org/10.1002/adom.202201691.
[24] Y. Blom, M.R. Vogt, C.M. Ruiz Tobon, R. Santbergen, M. Zeman, O. Isabella, Energy loss analysis of two-terminal tandem PV systems under realistic operating conditions—Revealing the importance of fill factor gains, Sol. RRL (2023) 2200579, http://dx.doi.org/10.1002/solr.202200579.
[25] A. Bag, R. Radhakrishnan, R. Nekovei, R. Jeyakumar, Effect of absorber layer, hole transport layer thicknesses, and its doping density on the performance of perovskite solar cells by device simulation, Sol. Energy 196 (2020) 177–182, http://dx.doi.org/10.1016/j.solener.2019.12.014.
[26] K. Wang, C. Liu, P. Du, L. Chen, J. Zhu, A. Karim, X. Gong, Efficiencies of perovskite hybrid solar cells influenced by film thickness and morphology of CH3NH3PbI3-xClx layer, Org. Electron. 21 (2015) 19–26, http://dx.doi.org/10.1016/j.orgel.2015.02.023.
[27] A. Baldridge, S. Hook, C. Grove, G. Rivera, The ASTER spectral library version 2.0, Remote Sens. Environ. 113 (4) (2009) 711–715, http://dx.doi.org/10.1016/j.rse.2008.11.007.
[28] S.S. Pal, F.H.C. van Loenhout, J. Westerhof, R. Saive, Understanding and benchmarking ground reflectors for bifacial photovoltaic yield enhancement, IEEE J. Photovolt. (2023) 1–10, http://dx.doi.org/10.1109/JPHOTOV.2023.3319592.
[29] M. Vogt, C.R. Tobon, A. Alcañiz, P. Procel, Y. Blom, A.N. El Din, T. Stark, Z. Wang, E.G. Goma, J. Etxebarria, H. Ziar, M. Zeman, R. Santbergen, O. Isabella, Introducing a comprehensive physics-based modelling framework for tandem and other PV systems, Sol. Energy Mater. Sol. Cells 247 (2022) 111944, http://dx.doi.org/10.1016/j.solmat.2022.111944.
[30] R. Santbergen, T. Meguro, T. Suezaki, G. Koizumi, K. Yamamoto, M. Zeman, GenPro4 optical model for solar cell simulation and its application to multijunction solar cells, IEEE J. Photovolt. 7 (3) (2017) 919–926, http://dx.doi.org/10.1109/JPHOTOV.2017.2669640.
[31] R. Siegel, Net radiation method for transmission through partially transparent plates, Sol. Energy 15 (3) (1973) 273–276, http://dx.doi.org/10.1016/0038-092X(73)90090-X.
[32] M. Zeman, J. van den Heuvel, M. Kroon, J. Willemen, B. Pieters, J. Krč, S. Solntsev, Advanced Semiconductor Analysis, Tech. rep., Delft University of Technology, Delft, 2019.
[33] M. Zeman, O. Isabella, S. Solntsev, K. Jäger, Modelling of thin-film silicon solar cells, Sol. Energy Mater. Sol. Cells 119 (2013) 94–111, http://dx.doi.org/10.1016/j.solmat.2013.05.037, Thin-film Photovoltaic Solar Cells. URL https://www.sciencedirect.com/science/article/pii/S0927024813002584.
[34] A. Ingenito, O. Isabella, S. Solntsev, M. Zeman, Accurate opto-electrical modeling of multi-crystalline silicon wafer-based solar cells, Sol. Energy Mater. Sol. Cells 123 (2014) 17–29, http://dx.doi.org/10.1016/j.solmat.2013.12.019, URL https://www.sciencedirect.com/science/article/pii/S0927024813006521.
[35] R. Santbergen, V. Muthukumar, R. Valckenborg, W. van de Wall, A. Smets, M. Zeman, Calculation of irradiance distribution on PV modules by combining sky and sensitivity maps, Sol. Energy 150 (2017) 49–54, http://dx.doi.org/10.1016/j.solener.2017.04.036.
[36] A. Calcabrini, R. Cardose, D. Gribnau, P. Babal, P. Manganiello, M. Zeman, O. Isabella, Time-varying, ray tracing irradiance simulation approach for photovoltaic systems in complex scenarios with decoupled geometry, optical properties and illumination conditions, Prog. Photovolt., Res. Appl. 31 (2) (2023) 134–148, http://dx.doi.org/10.1002/pip.3614.
[37] R. Perez, R. Seals, J. Michalsky, All-weather model for sky luminance distribution—Preliminary configuration and validation, Sol. Energy 50 (3) (1993) 235–245, http://dx.doi.org/10.1016/0038-092X(93)90017-I.
[38] C.A. Gueymard, Parameterized transmittance model for direct beam and circumsolar spectral irradiance, Sol. Energy 71 (5) (2001) 325–346, http://dx.doi.org/10.1016/S0038-092X(01)00054-8.
[39] P. Ricchiazzi, S. Yang, C. Gautier, D. Sowle, SBDART: A research and teaching software tool for plane-parallel radiative transfer in the earth's atmosphere, Bull. Am. Meteorol. Soc. 79 (10) (1998) 2101–2114, http://dx.doi.org/10.1175/1520-0477(1998)079<2101:SARATS>2.0.CO;2.
[40] Y. Blom, M. Ruben Vogt, H. Uzu, G. Koizumi, K. Yamamoto, O. Isabella, R. Santbergen, Exploring the potential of perovskite/perovskite/ silicon triple junction PV modules in two- and four-terminal configuration, Submitted to Sol. RRL (2024).
[41] T. hee Jung, H. eun Song, H. keun Ahn, G. hwan Kang, A mathematical model for cell-to-module conversion considering mismatching solar cells and the resistance of the interconnection ribbon, Sol. Energy 103 (2014) 253–262, http://dx.doi.org/10.1016/j.solener.2014.01.032, URL https://www.sciencedirect.com/science/article/pii/S0038092X14000504.
[42] Y. Blom, M. Ruben Vogt, O. Isabella, R. Santbergen, Method for bandgap interpolation of perovskite's spectral complex refractive index, Opt. Express 32 (3) (2024) 4365, http://dx.doi.org/10.1364/OE.509982.
[43] YBlom1999, YBlom1999/InterpolationNK_YB: Final, 2024, http://dx.doi.org/10.5281/zenodo.11367820.
[44] M. Bacha, A. Saadoune, I. Youcef, O. terghini, Design and numerical investigation of perovskite/silicon tandem solar cell, Opt. Mater. 131 (2022) 112671, http://dx.doi.org/10.1016/j.optmat.2022.112671, URL https://www.sciencedirect.com/science/article/pii/S0925346722007054.
[45] M. Kottek, J. Grieser, C. Beck, B. Rudolf, F. Rubel, World map of the Köppen-Geiger climate classification updated, Meteorol. Z. 15 (3) (2006) 259–263, http://dx.doi.org/10.1127/0941-2948/2006/0130.
[46] J. Ascencio-Vásquez, K. Brecl, M. Topič, Methodology of Köppen-Geiger-Photovoltaic climate classification and implications to worldwide mapping of PV system performance, Sol. Energy 191 (2019) 672–685, http://dx.doi.org/10.1016/j.solener.2019.08.072.
[47] C.A. Gueymard, V. Lara-Fanego, M. Sengupta, Y. Xie, Surface albedo and reflectance: Review of definitions, angular and spectral effects, and intercomparison of major data sources in support of advanced solar irradiance modeling over the Americas, Sol. Energy 182 (2019) 194–212, http://dx.doi.org/10.1016/j.solener.2019.02.040, URL https://www.sciencedirect.com/science/article/pii/S0038092X19301653.
[48] M.H. Futscher, B. Ehrler, Efficiency limit of perovskite/si tandem solar cells, ACS Energy Lett. 1 (4) (2016) 863–868, http://dx.doi.org/10.1021/acsenergylett.6b00405.
[49] A. Callies, M. Hanser, J.C. Goldschmidt, B. Bläsi, O. Höhn, Structuring of perovskite-silicon tandem solar cells for reduced reflectance and thermalization losses, Opt. Express 31 (12) (2023) 19428–19442, URL https://opg.optica.org/oe/abstract.cfm?URI=oe-31-12-19428.
[50] Y. Hu, Y. Chu, Q. Wang, Z. Zhang, Y. Ming, A. Mei, Y. Rong, H. Han, Standardizing perovskite solar modules beyond cells, Joule 3 (9) (2019) 2076–2085, http://dx.doi.org/10.1016/j.joule.2019.08.015, URL https://www.sciencedirect.com/science/article/pii/S2542435119304180.